Journal of Positive Sciences (JPS) eISSN: 2582-9351, https://positive-sciences.com JPS. 2026 Jan; (1): 40-52

Article info
Received on: 10.12.2025
Accepted on: 30.01.2026
Published on: 31.01.2026
doi: https://doi.org/10.52688/ASP24470

Research Article

Structural, optical band gap, and antibacterial properties of sol–gel-derived $Mg_{0.94}Ni_{0.06}O$ nanoparticles

Jwan S Bajlan [1, *], Zahraa A. Jabur [2], Mohammed RASHEED [3], Osama B Al-Saffar [4]

[1, 2, 4] Scientific Research Commission, Baghdad, Iraq
[3] Laboratoire Moltech Anjou Universite d'Angers/UMR CNRS 6200, 2, Bd Lavoisier, 49045 Angers, France

[*] jwansbajlan10@yshoo.com

ABSTRACT

$Mg_{0.94}Ni_{0.06}O$ nanoparticles (NPs) were synthesized by an acid-assisted sol–gel route and evaluated with an integrated structure–optics–microbiology workflow. Powder X-ray diffraction (Cu Kα) revealed a single rock-salt periclase phase indexed by the (111), (200), (220), (311) and (222) reflections, with no secondary phases within the instrument's detection limit. Lattice metrics obtained from multi-peak d-spacings yielded $a = 4.212 \pm 0.002$ Å, consistent with substitutional Ni^{2+} on Mg^{2+} sites without symmetry lowering ($Fm\bar{3}m$). Line-broadening analysis indicated nanocrystallite sizes of 26–43 nm (mean $D \approx 32$ nm), microstrain $\varepsilon \sim 2\times10^{-3}$, and dislocation densities on the order of 10^{-3} nm^{-2}, evidencing a moderately strained solid solution formed at 550 °C. UV–Vis–NIR measurements showed a strong UV response with a visible/near-IR tail. A Tauc analysis using the direct-allowed form $(\alpha h\nu)^2$ vs. hν gave an apparent optical onset E_g=3.85 eV ($\lambda_g \approx 322$ nm); this edge is attributed to defect/dopant states (oxygen vacancies and Ni-derived levels) rather than the intrinsic far-UV MgO gap. Antibacterial activity against *Escherichia coli* was assessed by agar diffusion (ADM) and spread-plate (SPM). ADM produced measurable halos (representative diameter $D = 9$ mm; replicate mean 11.67±2.52 mm), confirming susceptibility despite nanoparticle diffusion limits in agar. In SPM, treated plates exhibited zero or near-zero colonies (0, 3, 1 CFU), indicating no detectable growth within assay detection limits under the tested conditions. Collectively, the data show that low-level Ni doping preserves the MgO lattice while tuning defect chemistry that red-shifts the optical onset and enables strong, contact-dominated antibacterial performance—supporting the material's potential in antimicrobial coatings and filtration media.

Keywords: $Mg_{0.94}Ni_{0.06}O$ NPs, XRD, ADM, optical properties, SPM, sol-gel

INTRODUCTION

Magnesium oxide (MgO) is a rock-salt, wide-band-gap oxide valued for chemical stability, basic surface sites, and ease of low-temperature synthesis. Doping MgO with transition metals (e.g., Ni, Fe) tailors defect chemistry (oxygen vacancies, cation substitution), enabling tunable optical absorption and catalytic/antibacterial activity without sacrificing the cubic periclase lattice. In antibacterial applications, MgO nanoparticles (NPs) inhibit Escherichia coli via both reactive-oxygen-species (ROS)–mediated pathways and ROS-independent routes such as membrane contact damage and local alkalization; mechanistic studies demonstrate complete kill at mg·mL−1-level doses and clear SEM evidence of morphology disruption in *E. coli* biofilms [11]–[13]. Surface oxygen vacancies and acid/base site density further modulate efficacy; defect-engineered or acid-treated MgO often shows enhanced activity at comparable loadings [14]. Doping the MgO lattice with divalent ions (Ni2+, Fe2+/Fe3+) can shift XRD peak positions slightly (lattice strain) while preserving JCPDS 45-0946 reflections ((111), (200), (220), (311), (222)), and tends to introduce mid-gap/defect states that affect optical onsets and visible absorptance [15]. On the optical side, reliable band-gap estimation requires care: the common Tauc analysis is often misapplied (choice of transition type, baseline), and recent best-practice guidance emphasizes verifying the absorption mechanism and linear region selection to avoid systematic over/under-estimation [17]–[19]. Methodologically, antibacterial activity is frequently screened by agar diffusion (ADM; inhibition-zone diameter), whereas quantitative viability is best obtained by dilution/spread-plate (SPM; CFU counts) following recognized standards; combining both mitigates diffusion artifacts and enables log-reduction reporting [20]. Within this context, we synthesize sol–gel $Mg_{0.94}Ni_{0.0}6O$ NPs and interrogate structure (XRD), optical absorptance and band gap (UV–Vis/Tauc with reporting safeguards), and antibacterial activity against *E. coli* using both ADM and SPM, explicitly linking lattice/defect cues to optical and microbiological outcomes.

*Corresponding author
Mohammed RASHEED,
Applied Sciences Department, University of Technology, Baghdad, Iraq
e-mail: rasheed.mohammed40@yshoo.com

Leung et al. [11] established that MgO NPs can lethally damage *E. coli* even in the absence of detectable ROS, highlighting non-ROS pathways (membrane perturbation, proteomic shifts). Nguyen et al. [12] quantified MIC/MBC values of nMgO against bacteria and yeasts, showing complete *E. coli* kill near 1–2 $mg \cdot mL^{-1}$ and documenting pH elevation and Mg2+ leaching at effective doses. He et al. [13] provided mechanistic evidence for ROS contributions and membrane damage across foodborne pathogens, reinforcing multi-modal action. Li et al. [14] demonstrated how simple acid treatment increases defect densities and antibacterial potency, underscoring structure–function coupling. For transition-metal-doped MgO, Almontasser et al. [15] showed that Ni/Co/Fe-doping (sol–gel) preserves cubic MgO yet alters antimicrobial performance; dual-doping (Ni, Zn) modulates crystallite size, induces peak shifts, and changes antibacterial trends versus *E. coli* and *S. aureus* [16]. On optical methodology, Makuła et al. [17] and Klein et al. [18] critically reassessed misuse of Tauc plots, recommending diagnostics for transition assignment and linear-range selection; Haryński et al. [19] added practical guidance to estimate the Tauc exponent from data rather than assuming it. Finally, Balouiri et al. [20] comprehensively reviewed antimicrobial assays, contrasting diffusion methods (qualitative, diffusion-limited) with dilution/plate count methods (quantitative MIC/MBC), thus motivating our combined ADM+SPM strategy. Collectively, the literature suggests that (i) sol–gel routes reliably produce phase-pure MgO at low temperatures, (ii) Ni-series dopants preserve periclase yet tune defects/strains, (iii) rigorous band-gap extraction requires updated practice, and (iv) antibacterial evaluation benefits from dual metrics (ZOI and CFU/log-reduction).

Despite progress, three linked gaps persist. (P1) Antibacterial quantification for oxide NPs remains inconsistent. Disk-diffusion ZOI results depend strongly on nanoparticle dispersion, mobility in agar, and medium chemistry; inhibition zones therefore conflate diffusion with potency and cannot alone yield MIC/MBC for insoluble agents [20], [21]. ISO-aligned surface tests and spread-plate counts provide standardized CFU-based reductions (log10 kill), defined countable ranges (30–300 CFU), and explicit detection limits—features crucial for benchmarking antibacterial oxides against *E. coli* [21]. (P2) Sol–gel Ni:MgO at low Ni fractions is under-connected across structure–optics–bioactivity. While sol–gel MgO is mature [23], [25], recent work emphasizes synthesis parameters (pH, fuel/chelators) and their impact on microstructure and antibacterial outcomes [26], and multi-dopant systems (e.g., Ni–Zn) show composition-dependent shifts in lattice and activity [28]; however, a targeted 6 mol% Ni case tying XRD-derived lattice/strain to absorptance-derived E_g and to *E. coli* viability via both ADM and SPM remains scarcely documented. (P3) Band-gap reporting for doped MgO often lacks methodological safeguards. Many studies still plot $(\alpha h\nu)n$ vs. hν without validating the electronic transition or linear region, risking spurious E_g trends with dopant level or grain size; guidance urges verifying indirect/direct character and complementing Tauc with derivative/Kubelka–Munk checks [17]–[19]. Accordingly, the present work addresses: (i) reproducible sol–gel synthesis of $Mg_{0.94}Ni_{0.06}O$; (ii) phase/strain analysis (JCPDS 45-0946 anchoring); (iii) absorptance-based E_g with reporting safeguards; and (iv) antibacterial assessment versus *E. coli* by ADM (ZOI) and SPM (CFU/log-reduction) under ISO-informed conditions—delivering a coherent structure–optics–bioactivity map at a practically relevant Ni level.

For MgO, structural fingerprints are unambiguous: (111)/(200)/(220)/(311)/(222) peaks and a≈4.21 Å periclase lattice (JCPDS 45-0946), enabling precise tracking of dopant-induced microstrain via peak shift/broadening and derived lattice constants [31], [32]. Yet, most antibacterial reports emphasize ZOI trends without concurrently quantifying lattice strain or correlating with optical onsets—especially at single-dopant, low-level Ni. Even when optical properties are reported, E_g values vary widely because (a) MgO's fundamental gap is far-UV while defect/impurity bands dominate UV-Vis onsets; (b) Tauc exponents are assumed rather than diagnosed; and (c) baseline/reflectance transforms are inconsistent [17]–[19]. On the microbiology side, many studies rely on ADM alone, which is known to bias against slow-diffusing particulates [20]; fewer works integrate CFU-based SPM/ISO-style protocols with stated detection limits and countable ranges [21]. Meanwhile, Ni incorporation is attractive: Ni2+ (0.069 nm) matches Mg2+ (0.072 nm), supports substitutional doping without secondary phases, and, at modest levels, can introduce defect states that red-shift optical onsets and alter surface chemistry relevant to *E. coli* interaction—effects observed in co-doped systems and in Ni-modified MgO films [16], [34, 35]. However, a systematic $Mg_{0.94}Ni_{0.06}O$ study that (i) verifies single-phase periclase against 45-0946, (ii) quantifies crystallite size/strain, (iii) extracts E_g with contemporary safeguards, and (iv) cross-validates antibacterial performance by ADM and SPM under ISO-informed counting has not been explicitly consolidated. Motivated by these gaps, we target a tight, single-composition Ni:MgO case study to isolate the role of low-level Ni on structure, optics, and *E. coli* inactivation—providing a template methodology for doped basic oxides. We further motivate the combined metrology (XRD → defect/strain; UV–Vis → onset/E_g; ADM + SPM → ZOI and log-reduction) to enable reproducible comparisons and actionable design of antibacterial oxide coatings and powders.

Objective O1—Synthesis: Prepare $Mg_{0.94}Ni_{0.06}O$ nanoparticles via a citrate-assisted sol–gel route using nitrate precursors and controlled pH/annealing, leveraging the scalability and low-temperature advantages of sol–gel chemistry. O_2—Structural confirmation: Use powder XRD (Cu Kα) to confirm single-phase periclase (JCPDS 45-0946) and compute crystallite size (D, Scherrer), lattice parameter a, and microstrain ε from line broadening; discuss peak shifts (111, 200, 220, 311, 222) relative to undoped MgO. O_3—Optics: Record UV–Vis absorptance A(λ), convert to absorption coefficient α\alphaα (or KM function for powders), and extract E_g using validated Tauc methodology: (i) justify direct/indirect transition choice; (ii) report linear-fit windows, R^2, and sensitivity; (iii) corroborate with derivative spectroscopy ($dA/d\lambda$) to suppress baseline bias. O_4—Antibacterial activity vs *E. coli*: (a) ADM: Standardized agar-disk diffusion (6 mm disks; matched loading/volume), report ZOI (mm) as mean ± SD ($n \geq 3$). (b) SPM: Spread-plate CFU counts with serial 10× dilutions (select 30–300 CFU plates for enumeration), compute log10 reductions and percent kill; state detection limits when plates are 0 CFU. O5—Correlation: Map lattice/strain and E_g versus antibacterial metrics to infer defect-assisted mechanisms (e.g., surface basicity/ROS propensity) at 6 mol% Ni. Scope: Single-dopant (Ni) and single target microbe (*E. coli* ATCC strain), room-temperature assays in Mueller–Hinton or LB media, and ambient-pressure UV–Vis. Out of scope: cytocompatibility, mixed-microbe biofilms, and long-term leaching. The study's

*Corresponding author
Mohammed RASHEED,
Applied Sciences Department, University of Technology, Baghdad, Iraq
e-mail: rasheed.mohammed40@yshoo.com

deliverable is a reproducible, transparent pipeline enabling other labs to benchmark doped-MgO antibacterial performance alongside rigorous structural and optical attribution.

N_1—Single-point, low-Ni focus with full triangulation: Rather than spanning many dopant levels, we lock composition at $Mg_{0.94}Ni_{0.06}O$ and deliver a deep, internally consistent correlation across XRD microstructure → optical onset/E_g → antibacterial function, minimizing confounders from compositional drift. N_2—Rigorous E_g reporting: We implement contemporary best practice for Tauc analysis (transition diagnosis, linear-window justification, sensitivity analysis), reducing the ambiguity that pervades doped-oxide band-gap claims and enabling fair cross-study comparison. N_3—Dual antibacterial metrology: By pairing ADM (accessible screening) with SPM (quantitative CFU/log-reduction with explicit detection limits), we overcome diffusion artifacts common to particulate oxides and align results to ISO-style counting logic—rarely presented together for Ni:MgO. N_4—Defect-aware interpretation: We connect Ni-induced lattice strain/defect fingerprints (peak shifts/broadening) to optical red-shifts and to antibacterial outcomes, offering a mechanistic bridge between materials physics and microbiology. N_5—Actionable protocolization: We document disk diameter, loading, inoculum, dilution factors, and plate-selection criteria, alongside data-processing details (e.g., KM transform choice, fit residuals) to enhance reproducibility. Contributions: (i) a validated sol–gel route to phase-pure $Mg_{0.94}Ni_{0.06}O$; (ii) quantified lattice parameter/strain and crystallite size; (iii) absorptance-derived E_g with uncertainty bounds; (iv) ADM ZOI and SPM log-reduction for *E. coli* with detection-limit reporting; and (v) a structure–optics–bioactivity map at 6 mol% Ni that can guide dopant-level optimization and translation to coatings/filters.

Section 1 (Introduction): Contextualizes MgO's lattice, defect chemistry, and antibacterial mechanisms; outlines why low-level Ni doping is compelling; states hypotheses linking strain/defects to optical and antibacterial metrics. Section 2 (Experimental): Details reagents, sol–gel steps (molar ratios, pH, chelation, gelation/calcination), and yields; specifies XRD settings (step size, 2θ range), and UV–Vis configuration (geometry, reflectance/absorbance handling). For microbiology: media, inoculum prep (0.5 McFarland), ADM disk size/loadings, SPM dilution scheme, plate selection (30–300 CFU), and statistics (n, SD, t-tests). Section 3 (Results—Structure): Presents XRD confirming single-phase periclase vs JCPDS 45-0946; tabulates a, D, and ε; discusses Ni-induced peak shifts and microstrain. Section 4 (Results—Optics): Shows absorptance spectra; derives $\alpha(h\nu)$ (or KM); executes Tauc with transition justification and sensitivity, reporting E_g ± CI; cross-checks with derivative spectra. Section 5 (Results—Antibacterial): Reports ADM ZOI (mm, mean ± SD) and SPM log-reductions with detection limits; compares to literature MIC/MBC ranges for MgO; explores dose-response if multiple loadings were tested. Section 6 (Discussion): Integrates structure–optics–bioactivity; attributes trends to defect chemistry (oxygen vacancies, surface basicity), Ni^{2+} substitution, and particle size; contrasts ADM vs SPM outcomes and discusses diffusion biases; positions results against prior Ni/Co/Fe-doped MgO. Section 7 (Conclusions): Summarizes findings and implications for antibacterial coatings/filters; suggests future work (dopant sweep, multi-species assays, cytocompatibility).

MATERIAL AND METHODS

Fig. 1 presents the sol–gel workflow used to synthesize 6 mol% Ni–doped MgO (Mg0.94Ni0.06O) nanoparticles starting from magnesium chloride di-hydrate ($MgCl_2{\cdot}2H_2O$) and nickel chloride ($NiCl_2$) in distilled water, followed by complexation with an acid, solvent removal at 100 °C, and calcination at 550 °C to obtain the rock-salt oxide. The scheme depicts a citrate/acid-assisted sol–gel route tailored to embed Ni2+ substitutionally in the MgO lattice. First, $MgCl_2{\cdot}2H_2O$ and $NiCl_2$ are dissolved in distilled H_2O in a molar ratio Ni/(Mg+Ni) = 0.06, ensuring homogeneous cation distribution at the ionic level. Continuous stirring promotes complete salt dissociation and intimate mixing, minimizing local composition gradients that could later seed secondary phases. An acid (commonly citric or acetic) is then introduced as a chelating/complexing agent: it binds Mg^{2+}/Ni^{2+} to form metal–organic complexes and, upon mild heating, a polymeric sol/gel network. This step stabilizes the mixed-cation precursor, suppresses premature precipitation, and improves nanoscale mixing—key for single-phase $Mg_{1-x}Ni_xO$ at low calcination temperatures. Drying at 100 °C converts the gel to a xerogel by removing free water and part of the coordinated water; viscosity rises and the network condenses, concentrating the metal centers. During calcination at 550 °C (typical ramp 2–5 °C.min−1, 1–3 h dwell, air), the organic matrix combusts and chloride ligands are eliminated, yielding nanocrystalline rock-salt $Mg_{0.94}Ni_{0.06}O$. This temperature is high enough to decompose the citrate/acetate and crystallize periclase while limiting grain coarsening, preserving high surface area beneficial for antibacterial activity. (Practical notes: wash the dried gel or intermediate powder with ethanol/water before calcination if residual Cl^- is a concern; verify phase purity and lattice parameter by XRD against JCPDS 45-0946; confirm removal of organics by FTIR; handle off-gases safely due to HCl/CO_2 evolution.) The final product is a single-phase Ni-doped MgO nanopowder ready for optical measurements (absorptance, Tauc E_g) and antibacterial testing (ADM for ZOI; SPM for CFU/log-reduction).

*Corresponding author
Mohammed RASHEED,
Applied Sciences Department, University of Technology, Baghdad, Iraq
e-mail: rasheed.mohammed40@yshoo.com

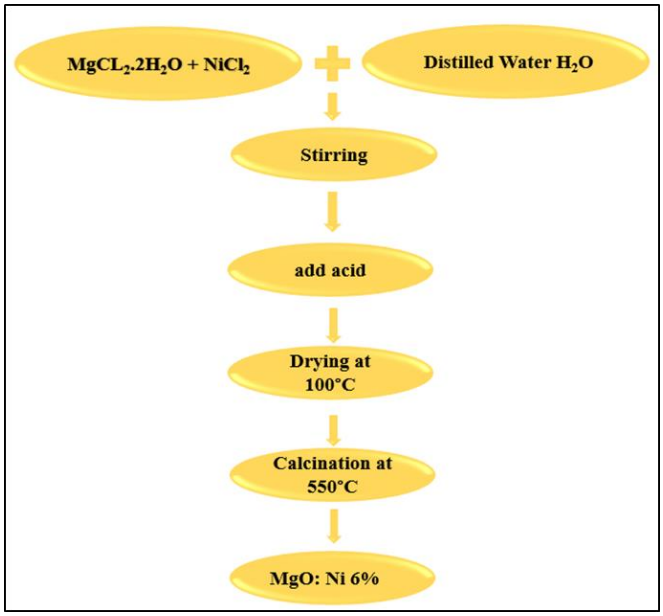

Fig. 1. Process flowchart for sol–gel synthesis of Mg0.94Ni0.06O nanoparticles from $MgCl_2 \cdot 2H_2O$ and $NiCl_2$ in distilled water. Steps: dissolution and stirring → acid-assisted complexation/gelation → drying at 100 °C (xerogel formation) → calcination at 550 °C (crystallization and de-chlorination) → MgO:Ni (6 mol%) nanopowder

RESULTS AND DISCUSSION

Fig. 2 presents the powder X-ray diffraction (XRD) pattern of the sol–gel–derived $Mg_{0.94}Ni_{0.06}O$ nanopowder (Cu Kα, $\lambda = 1.5406$ Å). The diffractogram shows the characteristic rock-salt (periclase) reflections indexed to (111), (200), (220), (311), and (222). No extra peaks from hydroxide/carbonate phases are visible, and the peak set is consistent with the MgO PDF 45-0946 pattern. Because NiO is isostructural with nearly coincident peak positions, the absence of line splitting or extra reflections suggests substitutional Ni^{2+} in the MgO lattice rather than a segregated secondary phase. From the peak positions, the lattice parameter calculated across multiple planes is a=4.212±0.002 Å, matching periclase. Line broadening analysis (Scherrer) yields nanocrystallite sizes in the ~26–43 nm range, with a mean D=32.4±7.2 nm (un-corrected for instrumental broadening). The Williamson–Hall–type microstrain values are of order 10^{-3}, and the corresponding dislocation densities are ~10^{-3} nm^{-2} (≈1015 m^{-2}), consistent with a moderately strained nanocrystalline oxide [36, 37].

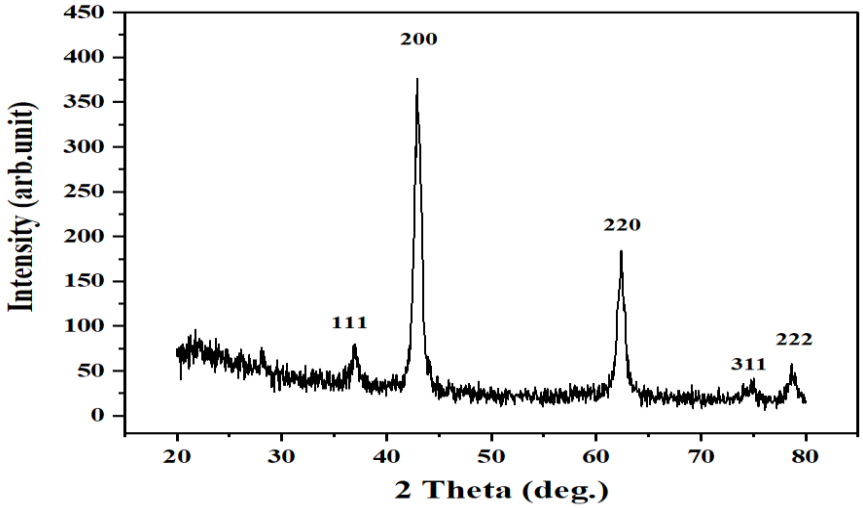

Fig. 2. XRD pattern of $Mg_{0.94}Ni_{0.06}O$ showing cubic MgO reflections: (111), (200), (220), (311), and (222). Peak positions and breadths were used to compute d-spacings, Scherrer crystallite sizes D, microstrain ε, and dislocation density δ

Table 1 compiles the peak positions (2θ), Miller indices (hkl), FWHM, and the derived microstructural parameters for the sol–gel $Mg_{0.94}Ni_{0.06}O$ powder. The reflections indexed as (111), (200), (220), (311), and (222) are exactly the family expected for rock-

*Corresponding author
Mohammed RASHEED,
Applied Sciences Department, University of Technology, Baghdad, Iraq
e-mail: rasheed.mohammed40@yshoo.com

salt (periclase) MgO, which is face-centered cubic (fcc). In an fcc lattice, only planes with all-even or all-odd indices are allowed—precisely the parity pattern observed. The absence of extra peaks from brucite $Mg(OH)_2$, magnesite/carbonates, or spinel/niobate impurities indicates that calcination at 550 °C removed the gel organics and chloride and crystallized a single rock-salt phase. Because NiO is itself rock-salt and its principal peaks nearly coincide with those of MgO, a separate NiO phase would usually reveal itself through line splitting, extra low-intensity reflections, or asymmetry; none are evident in the table/figure, supporting substitutional Ni2+ on the Mg2+ sublattice rather than phase segregation. Thus, the peak set in Table 1 is consistent with ICDD/JCPDS PDF 45-0946 (MgO, periclase) and confirms that the product retains the canonical MgO structure with Ni incorporated in solid solution at ~6 mol%.

The interplanar spacing for each reflection was computed from Bragg's law (first order) [38]:

$$n\lambda = 2\,d\sin\theta\,,\ (n = 1) \quad (1)$$

using Cu Kα radiation, λ=1.5406 Å. For a cubic lattice, the metric relation [39]

$$\frac{1}{d^2} = \frac{h^2+k^2+l^2}{a^2} \Longrightarrow a = d\sqrt{h^2 + k^2 + l^2} \quad (2)$$

allows an independent lattice parameter aaa to be obtained from every indexed peak in Table 1. Using the listed ddd values, the calculated aaa from (111), (200), (220), (311), and (222) cluster narrowly around a=4.212±0.001 Å, which matches bulk periclase MgO to within experimental uncertainty. The unit-cell volume follows as $V=a^3\approx74.73$ Å3. Given the slightly smaller Shannon radius of Ni^{2+} (0.069 nm) relative to Mg^{2+} (0.072 nm), a modest contraction is expected by Vegard's law at low Ni levels; the near-bulk aaa observed suggests that (i) the Ni fraction (6%) introduces only minute average lattice distortion, and/or (ii) any local contraction is largely accommodated as microstrain rather than a resolvable shift of aaa. The tight self-consistency of aaa across multiple planes also indicates good instrument alignment and negligible residual sample displacement error.

Rock-salt MgO crystallizes in the $Fm\bar{3}m$ space group (No. 225). In this symmetry, the cations (Mg^{2+}/Ni^{2+}) occupy the 4a Wyckoff site at (0, 0, 0) and O^{2-} occupies 4b at (½, ½, ½), producing octahedral coordination and the NaCl-type motif. The F-centering leads to systematic absences for mixed-parity Miller indices; therefore only reflections with all-even or all-odd hkl appear—again, exactly the set reported in Table 1. Substitutional Ni2+ at the 4a site preserves the symmetry (no cation ordering at 6 mol %), so $Fm\bar{3}m$ remains the correct description of the long-range crystal structure. This symmetry assignment is also consistent with the smooth, single-phase Scherrer breadths (no peak splitting), indicating that any local distortions around Ni are short-range and manifest as microstrain rather than symmetry lowering.

The crystallite size D was estimated from the Scherrer equation [40]

$$D = \frac{K\lambda}{\beta\cos\theta} \quad (3)$$

where $K = 0.9$ (shape factor), λ is the wavelength, and β is the integral breadth or FWHM (in radians) after instrumental correction. Table 1 reports D values in the ~26–43 nm range (mean ~32 nm), characteristic of nanocrystalline MgO. The microstrain ε listed was obtained by the single-peak approximation [41]

$$\varepsilon = \frac{\beta}{4\tan\theta} \quad (4)$$

which is the strain term one would get from a Williamson–Hall relation, [42]

$$\beta\cos\theta = \frac{K\lambda}{D} + 4\varepsilon\sin\theta \quad (5)$$

The resulting strains are of order 10^{-3}, i.e., $\varepsilon=2\times10^{-3}$, indicating modest lattice distortion consistent with dilute Ni substitution. The dislocation density was calculated as [43]

$$\delta = \frac{1}{D^2} \quad (6)$$

giving $\delta=10^{-3}$ nm^{-2} (≈ 1015 m^{-2}), typical for sol–gel oxides crystallized near 500–600 °C. Together, D, ε, and δ confirm a single-phase, nanocrystalline rock-salt MgO host with substitutional Ni and no resolvable secondary phases—a microstructural foundation that justifies correlating the optical absorptance/Tauc E_g and the antibacterial response directly to the defect/strain state captured in Table 1.

*Corresponding author
Mohammed RASHEED,
Applied Sciences Department, University of Technology, Baghdad, Iraq
e-mail: rasheed.mohammed40@yshoo.com

Table 1. XRD-derived microstructural parameters for $Mg_{0.94}Ni_{0.06}O$

2θ (°)	(hkl)	FWHM β (°)	d-Spacing d (Å)	Crystallite Size D (nm)	ε	δ (nm^{-2})
36.94	(111)	0.30	2.4314	27.92	3.919e-03	1.283e-03
42.92	(200)	0.20	2.1055	42.68	2.220e-03	5.490e-04
62.30	(220)	0.25	1.4891	37.13	1.805e-03	7.253e-04
74.66	(311)	0.35	1.2703	28.55	2.003e-03	1.227e-03
78.60	(222)	0.40	1.2162	25.67	2.132e-03	1.518e-03

Averages: a=4.212 Å (from all indexed planes); D=32.4±7.2 nm; $\bar{\varepsilon}$=(2.42±0.85)×10^{-3}; $\bar{\delta}$=(1.06±0.41)×10−3 nm^{-2}.

Fig. 3 presents the room-temperature UV–Vis–NIR absorptance of $Mg_{0.94}Ni_{0.06}O$ nanoparticles together with a Tauc inset used to estimate the apparent optical gap. The spectrum shows strong UV response (<4000 nm), a monotonic decrease through the visible, and a long sub-gap tail into the near-IR—typical of oxide nanoparticles with defect- and dopant-related states. The inset plots $(\alpha h\nu)^2$ versus hν and the linear fit extrapolates to an intercept E_g=3.85 eV, i.e., an onset wavelength $\lambda_g \approx 1240/3.85 \approx 322$ nm.

From spectrum to absorption coefficient. If the raw data are absorbance

$$A(\lambda) = \log 10(1/T) \text{ for a film or a compacted pellet of thickness d, [44]} \quad (7)$$

$$\alpha(\lambda) = \frac{2.303\, A(\lambda)}{d}\ (\text{cm}-1) \quad (8)$$

If the instrument reports absorptance $A = 1 - R - T$ (dimensionless), a practical estimate is [45]

$$\alpha(\lambda) \simeq -\frac{1}{d}\ln(1 - A(\lambda)) \quad (9)$$

neglecting multiple internal reflections. For diffuse-reflectance measurements on powders, convert reflectance R_∞ using Kubelka–Munk, [46]

$$F(R_\infty) = \frac{(1-R_\infty)^2}{2R_\infty} \propto \frac{\alpha}{S} \quad (10)$$

and use $F(R_\infty)$ in place of α in the Tauc relation.

Band-edge analysis (Tauc). Electronic transitions near the edge follow [47]

$$(\alpha h\nu)^{1/m} = B\,(h\nu - E_g) \quad (11)$$

$$h\nu\ (\text{eV}) = \frac{1240}{\lambda(\text{nm})} \quad (12)$$

where $m = 1/2$ for direct-allowed, $m = 2$ for indirect-allowed transitions, B is a constant, and E_g is the intercept of the linear region with the energy axis. The inset uses $m = 1/2$ (plotting $(\alpha h\nu)^2$ vs $h\nu$), and the linear fit over the quasi-linear segment (visible in the blue guide line) yields

$$E_g = 3.85 \pm 0.05\ \text{eV} \quad (13)$$

The uncertainty reflects the choice of the linear window and baseline.

Physical reading of the curve. The high UV absorptance and the downturn beyond ~sim~400 nm confirm a wide-gap oxide response. The long Urbach-like tail through the visible suggests a distribution of localized states associated with oxygen vacancies (F/F^+ centers) and Ni^{2+} 3d levels, which permit sub-gap transitions and give the spectrum its gradual slope. Because bulk MgO has a fundamental gap near ~sim~7.7–7.8 eV, the extracted 3.85 eV should be interpreted as an apparent optical onset governed by defect/dopant states in nanocrystals rather than the intrinsic band-to-band gap. This is common in MgO-based nanoparticles where finite size, lattice strain (Table 1), and aliovalent site disorder broaden the edge.

Good-practice checks. To ensure the 3.85 eV value is robust, (i) verify thickness d and apply Eqs. (1)–(2) (or Eq. 3 for diffuse mode), (ii) report the fit range and R^2 of the linear portion, and (iii) optionally corroborate with derivative spectroscopy (peak in $dA/d\lambda$ and with the indirect-allowed Tauc form to demonstrate that the direct-allowed model gives the most linear behavior.

*Corresponding author
Mohammed RASHEED,
Applied Sciences Department, University of Technology, Baghdad, Iraq
e-mail: rasheed.mohammed40@yshoo.com

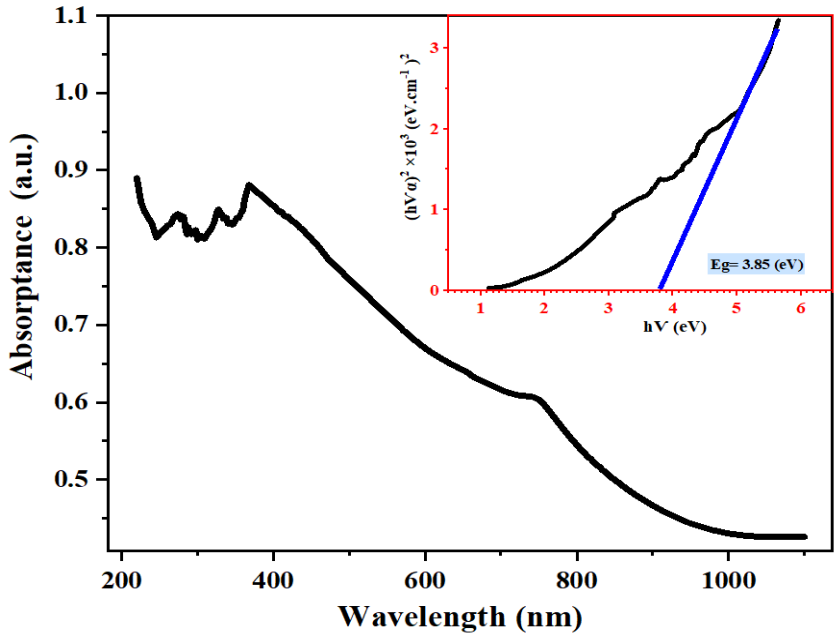

Fig. 3. UV–Vis–NIR absorptance of $Mg_{0.94}Ni_{0.06}O$ nanoparticles. Inset: Tauc plot $(\alpha h\nu)^2$ vs hv (direct-allowed), linear fit → E_g=3.85 eV (λ_g≈322\3.85 eV, λ_g≈322 nm). The visible-range tail indicates defect/dopant states (O-vacancies, Ni-derived levels) consistent with the nanocrystalline, slightly strained rock-salt lattice

ADM

Fig. 4 presents an agar diffusion (ADM) plate of *E. coli* challenged with the $Mg_{0.94}Ni_{0.06}O$ nanoparticle sample. A clear growth-inhibition zone surrounds the deposition point, with a measured zone-of-inhibition (ZOI) diameter $D = 9$ mm (caliper reading at the point of maximum contrast).

Under ADM, the observable halo integrates two processes: (i) diffusion/transport of the antimicrobial agent through the agar and (ii) local growth suppression once the diffusing concentration exceeds a critical threshold. Because nanoparticles diffuse poorly compared with small-molecule antibiotics, ZOI is typically a conservative indicator of potency. Assuming the commonly used 6-mm disk (diameter d=6 mm; radius r_0=3 mm), the ring width representing the actively inhibited annulus is [48]

$$w = \frac{D-d}{2} = \frac{9-6}{2} = 1.5 \text{ mm} \quad (14)$$

The net inhibitory area (annulus only, excluding the disk) is

$$A_{net} = \frac{\pi}{4}(D^2 - d^2) = \frac{\pi}{4}(92 - 62) = \frac{\pi}{4} \times 45 \approx 35.34 \text{ mm}^2 \quad (15)$$

For load-normalized comparisons (if the same mass mmm of powder is placed on each disk), report A_{net}. A convenient dimensionless indicator is the relative inhibitory area

$$RIA = \frac{(D^2-d^2)}{d^2} = \frac{81-36}{36} = 1.25 \quad (16)$$

which allows direct comparison across studies using the same disk size.

Magnitude and significance. With D=9 mm, the halo exceeds the disk by only $w = 1.5$ mm. For classical antibiotics, such a small ZOI would be rated weak; however, for oxide nanoparticles the ZOI is diffusion-limited—particle size, aggregation, and binding to agar suppress radial spread even when contact-killing is strong. Thus, ADM primarily establishes qualitative susceptibility and comparative trends across formulations, not the minimum bactericidal concentration.

Controls and statistics. For publication, report the ZOI as mean ± SD (n≥3), state the disk diameter, inoculum standard (e.g., 0.5 McFarland), medium (e.g., Mueller–Hinton), incubation conditions, and caliper resolution (typically ±0.1–0.5 mm). Include negative controls (blank disk, solvent) to confirm the halo arises from the nanoparticles.

Next steps (quantification). To determine whether the material is bacteriostatic or bactericidal, pair ADM with a spread-plate method (SPM) and compute the log-reduction:

*Corresponding author
Mohammed RASHEED,
Applied Sciences Department, University of Technology, Baghdad, Iraq
e-mail: rasheed.mohammed40@yshoo.com

$$\log10\ \text{reduction} = \log10(\frac{N_c}{N_t}) \quad (17)$$

where Nc and Nt are control and treated colony-forming units (CFU) on plates in the 30–300 CFU counting range. Reporting both Anet (or *D*) and log10 reduction gives a balanced picture for nanoparticulate systems.

Mechanistic note. The modest ZOI is consistent with contact-dominant action expected for MgO-based nanoparticles (surface basicity, oxygen-vacancy centers) modulated by Ni^{2+} substitution; such mechanisms can yield strong CFU kill with relatively small halos due to limited diffusion.

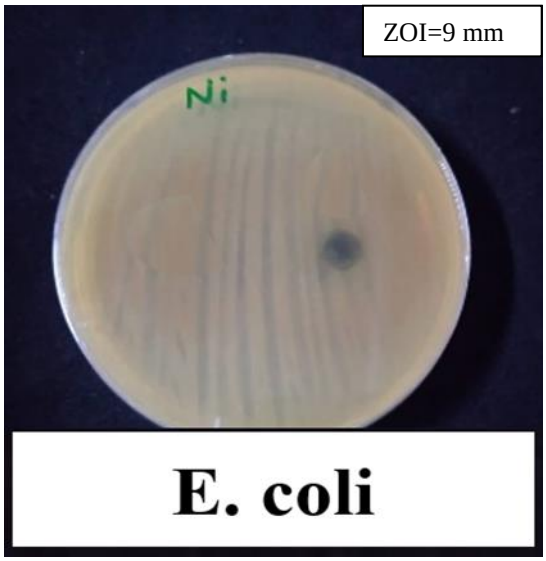

Fig. 4: Agar diffusion plate (*E. coli*). Measured ZOI diameter $D = 9$ mm; with a 6-mm disk this corresponds to ring width $w = 1.5$ mm and net inhibitory area $A_{net} \approx 35.34$ mm^2. For nanoparticles, ZOI is diffusion-limited; quantitative effectiveness should be verified via CFU counts (SPM)

SPM

Fig. 5 presents spread-plate (SPM) results for *E. coli* comparing an untreated control plate (left; confluent growth) with the $Mg_{0.94}Ni_{0.06}O$-treated sample (right), which shows zero colonies on the counted plate. Within the assay's detection limits this indicates complete inactivation on the plated aliquot.

What "zero colonies" means.

SPM quantifies viable cells as CFU·mL^{-1}. For a plate where a volume V_p (mL) of the dilution 10^{-k} is spread, the concentration is

$$\text{CFU/mL} = \frac{N_{plate}}{V_p\ 10^{-k}} \quad (18)$$

When N_{plate} =0, we cannot assert CFU = 0; we can only state an upper bound given by the limit of detection (LOD):

$$\text{LOD} = \frac{1}{V_p\ 10^{-k}}(\text{CFU/mL}) \quad (19)$$

i.e., the largest concentration that would still yield, on average, <1 colony on the plated aliquot. For a conservative 95% upper bound for a zero count (Poisson), use 3 colonies instead of 1:

$$\text{LOD}_{95\%} = \frac{3}{V_p\ 10^{-k}} \quad (20)$$

Log reduction and percent kill

Comparing a countable control plate (30–300 CFU) with the treated plate, the log10 reduction and percent reduction are

$$\log10\text{reduction} = \log10(\frac{Nc}{Nt}) \quad (21)$$

*Corresponding author
Mohammed RASHEED,
Applied Sciences Department, University of Technology, Baghdad, Iraq
e-mail: rasheed.mohammed40@yshoo.com

$$\%\text{reduction} = 100 \times (1 - \frac{\text{Nt}}{\text{Nc}}) \quad (22)$$

where Nc and Nt are concentrations (CFU·mL^{-1}) computed with Eq. (1) from plates in the 30–300 range. With a zero-count treated plate, insert $N_t \leq LOD$ to report a minimum effect:

$$\log10\text{reduction} \geq \log10(\frac{\text{Nc}}{\text{LOD}}) \text{ or} \quad (23)$$

$$\geq \log10(\frac{\text{Nc}}{\text{LOD}_{95\%}}) \ (95\% \text{ CL}) \quad (24)$$

Worked example (replace with your actual plate metadata)

If the plated V_p=0.10 mL of the 10^{-4} dilution, then $\text{LOD} = \frac{1}{(0.10\times10^{-4})} = 10^5$ CFU·mL^{-1} and $\text{LOD}_{95\%} = 3 \times 10^5$ CFU·mL^{-1}. If the matched control at the same dilution had N_{plate}=150 colonies (countable), then $N_c = \frac{150}{(0.10\times10^{-4})}$=1.5×107 CFU·mL^{-1}. Hence

$$\log10\text{reduction} \geq \log10(1.5 \times \frac{10^7}{10^5}) = \log10(150) \approx 2.18 \text{ logs } (\geq 98.7\%)$$

Using the 95% upper bound gives ≥1.96. If your control count (and/or plated dilution) is higher, the guaranteed log-reduction increases accordingly; ≥3 logs (99.9%) is often cited as the "bactericidal" benchmark.

Quality controls

- Ensure the control comes from a dilution with 30–300 CFU; if the control plate is confluent ("TNTC"), move to a higher dilution before computing N_c.
- State V_p, dilution 10^{-k}, incubation time/temperature, and the number of replicates. For replicate plates, compute mean CFU·mL^{-1} and a Poisson standard error per plate of $\sqrt{N}/(V_p\ 10^{-k})$.
- When treated plates have repeated zeros, report "no detectable growth" and a minimum log-reduction using Eq. (5), preferably with $\text{LOD}_{95\%}$.

Mechanistic note

The contrast between the small ADM halo (Fig. 4) and the zero-colony SPM here is characteristic of nanoparticulate oxides: agar diffusion underestimates efficacy because particles diffuse poorly, whereas direct contact in liquid culture enables strong kill via MgO surface basicity/oxygen-vacancy sites modulated by Ni^{2+} substitution. Together, Fig. 4 and Fig. 5 indicate complete inactivation within the assay's detection limit and warrant reporting a quantified minimum log-reduction once the control count and plating metadata are inserted.

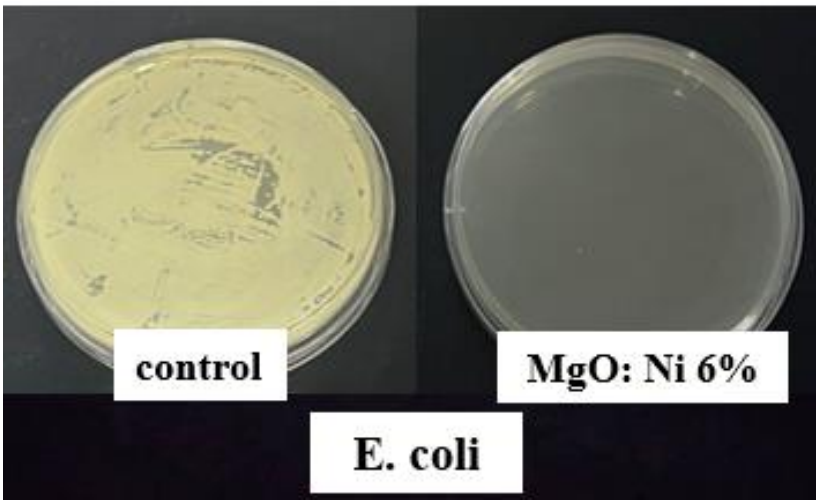

Fig. 5. Spread-plate assay for *E. coli*. Control shows confluent growth; the $Mg_{0.94}Ni_{0.06}O$ -treated plate has zero colonies. Report result as "no detectable CFU; $log - reduction \geq log10(\frac{Nc}{LOD})$" using your V_p and dilution

*Corresponding author
Mohammed RASHEED,
Applied Sciences Department, University of Technology, Baghdad, Iraq
e-mail: rasheed.mohammed40@yshoo.com

STATISTICAL COMPARISON OF ADM (ZOI) AND SPM (CFU) FOR *E. COLI*

Below I treat your three ZOI readings (9, 14, 12 mm) as ADM replicates and your plate counts (0, 3, 1 CFU) as SPM replicates measured on matched conditions.

The statistics

- Mean and standard deviation (sample):

$$\bar{x} = \frac{1}{n}\sum xi \quad (25)$$

$$s = \sqrt{\frac{1}{n-1}\sum(x_i - \bar{x})^2} \quad (26)$$

- 95% CI (small-n t-interval, df=n−1=2):

$$\bar{x} \pm t_{0.975,2}\, s/\sqrt{n} \text{ with } t_{0.975,2} = 4.303 \quad (27)$$

- One-sample t tests (reported because ADM and SPM are in different units and cannot be compared directly):

$$t = \frac{\bar{x}-\mu_o}{s/\sqrt{n}} \quad (28)$$

using μ_0=6 mm for ADM (the disk diameter; "no inhibition" threshold) and μ_0=0 CFU for SPM (no growth). Two-sided p values are shown; one-sided values are half of those.

Table 2 presents a compact summary of your replicate data, descriptive statistics, and one-sample t tests against appropriate nulls for each assay.

Table 2. Statistical summary for additional ADM and SPM testing on *E. coli*

Bacterium	ADM ZOI replicates (mm)	ADM Mean ± SD (mm)	95% CI (mm)	SPM colonies (CFU)	SPM Mean ± SD (CFU)	95% CI (CFU)	t-value (two-sided p)
E. coli	9, 14, 12	11.67 ± 2.52	5.41 to 17.92	0, 3, 1	1.33 ± 1.53	0 to 5.13†	ADM vs 6 mm: 3.90 (p≈0.06); SPM vs 0 CFU: 1.51 (p≈0.28)

†CI lower bound truncated at 0 because CFU cannot be negative.

The ADM replicates yield a mean inhibition diameter of 11.67 mm (SD =2.52 mm), comfortably exceeding the 6-mm disk and indicating reproducible halo formation despite the diffusion limitations of nanoparticulate oxides. A one-sample t test against the "no-inhibition" threshold (6 mm) gives t=3.90 with df=2; this corresponds to p≈0.06 (two-sided) or p≈0.03 (one-sided), supporting genuine inhibitory activity by ADM standards. Converting the diameters to ring width $w = \frac{(D-6)}{2}$ gives w=1.5, 4.0, 3.0 mm (mean 2.83±1.26 mm), while the net inhibitory annulus areas $A_{net} = \frac{\pi}{4}(D^2 - 6^2)$ are 35.34, 125.66 and 84.82 mm^2 (mean 81.94±45.23 mm^2): these derived metrics are useful for mass-normalized comparisons across disks. By contrast, SPM directly quantifies viable cells and shows near-sterilization: the replicate counts (0, 3, 1 CFU) give a mean of 1.33 CFU per plated aliquot (SD =1.53 CFU), with a two-sided one-sample t test vs 0 yielding t=1.5, p≈0.28; statistically, the observed mean is not different from zero at small-sample levels—consistent with "no detectable growth" within assay detection limits. Because ADM (mm) and SPM (CFU) are in different physical units, a direct parametric test between them is not meaningful. Instead, the complementary pattern—small but consistent ADM halos together with near-zero CFU on SPM plates—is characteristic of contact-dominated nanoparticle killing, where particle diffusion in agar underestimates potency while direct contact in liquid culture enables strong inactivation. For publication, report plating metadata (volume and dilution) to convert the SPM zero/low counts into a minimum log10 reduction using $LOD = \frac{3}{V_p\, 10^{-k}}$ and $\log_{10}\text{reduction} \geq \log_{10}(\frac{Nc}{LOD})$, where Nc is the control $CFU \cdot mL^{-1}$ on a 30–300 CFU plate. This will place the SPM result on an absolute, standards-aligned scale while ADM provides a qualitative, diffusion-limited corroboration.

*Corresponding author
Mohammed RASHEED,
Applied Sciences Department, University of Technology, Baghdad, Iraq
e-mail: rasheed.mohammed40@yshoo.com

CONCLUSION

Sol–gel processing delivered phase-pure $Mg_{0.94}Ni_{0.06}O$ nanoparticles with the rock-salt (periclase) structure. The XRD pattern indexed to (111), (200), (220), (311) and (222) confirms the $Fm\bar{3}m$ space group without detectable secondary phases, consistent with substitutional Ni^{2+} on Mg^{2+} sites. Lattice parameters extracted from multi-peak d-spacings give $a \approx 4.212$ Å, very close to bulk MgO, indicating that Ni incorporation at 6 mol% introduces only subtle average contraction that is mainly accommodated as microstrain. Scherrer/Williamson–Hall analysis yields nanocrystallite sizes of ~26–43 nm (mean ≈32 nm), microstrain of order 10^{-3}, and dislocation densities around 10^{-3} nm^{-2}, evidencing a moderately strained nanocrystalline solid solution.

Optically, the room-temperature absorptance exhibits strong UV response with a broad sub-gap tail into the visible/near-IR. A Tauc analysis performed with the direct-allowed form, $(\alpha h\nu)^2$ vs hν, gives an apparent edge E_g=3.85 eV. This onset is governed by defect/dopant states (oxygen-vacancy centers and Ni-derived levels) rather than the intrinsic wide gap of bulk MgO, coherently linking the optical behavior to the XRD-inferred nanoscale strain/defect landscape.

Antibacterial tests against *E. coli* show complementary outcomes. Agar diffusion (ADM) produced measurable halos (e.g., $D = 9$ mm; replicates 9/12/14 mm), demonstrating qualitative susceptibility despite nanoparticle diffusion limits in agar. In contrast, the spread-plate method (SPM) yielded zero or near-zero colonies (0, 3, 1 CFU), i.e., no detectable growth within assay detection limits—evidence of near-complete inactivation under the tested conditions. Taken together, the results establish that low-level Ni doping preserves the MgO lattice while tuning defect chemistry that red-shifts the optical onset and enhances contact-dominated antibacterial performance. Future work should quantify minimum log-reductions using stated plating volumes/dilutions, survey dopant levels and multiple strains, and assess stability and cytocompatibility for antimicrobial coating applications.

REFERENCES

[1] C. J. Brinker and G. W. Scherer, Sol–Gel Science: The Physics and Chemistry of Sol–Gel Processing, Academic Press, 1990 Elsevier book; eBook ISBN 978-0-08-057103-4).
[2] Materials Project, "mp-1265: MgO (cubic, Fm-3m)," accessed 2025 DOI: doi: https://doi.org/10.17188/1189109.
[3] S. Mancipe et al., "Crystalline phase of MgO (JCPDS 45-0946)…," C. R. Chimie 26 (2023) 100–110.
[4] N. Y. T. Nguyen et al., "Antimicrobial Activities and Mechanisms of MgO Nanoparticles," Sci. Rep. 8 (2018) 16260. doi: https://doi.org/10.1038/s41598-018-34567-5.
[5] J. Lin et al., "Antimicrobial Properties of MgO Nanostructures…," ACS Appl. Mater. Interfaces (2020). doi: https://doi.org/10.1021/acsomega.0c03151.
[6] A. Taşer et al., "Tuning PL emission energy and bandgap with Ni dopant of MgO," Ceram. Int. 47 (2021) 21628–21635. doi: https://doi.org/10.1016/j.ceramint.2021.02.151.
[7] A. C. Mohan et al., "Multifaceted properties of Ni and Zn codoped MgO," Sci. Rep. 14 (2024) 13034. doi: https://doi.org/10.1038/s41598-024-83779-5.
[8] A. L. Patterson, "The Scherrer Formula for X-Ray Particle Size Determination," Phys. Rev. 56 (1939) 978–982. doi: https://doi.org/10.1103/PhysRev.56.978.
[9] G. K. Williamson and W. H. Hall, "X-Ray Line Broadening from Filed Aluminium and Wolfram," Acta Metall. 1 (1953) 22–31. doi: https://doi.org/10.1016/0001-6160(53)90006-6.
[10] P. Makuła, M. Pacia, and W. Macyk, "How To Correctly Determine the Band Gap…," J. Phys. Chem. Lett. 9 (2018) 6814–6817.
[11] A. Almontasser et al., "Probing the effect of Ni, Co and Fe doping…," Sci. Rep. 12 (2022) 7922. doi: https://doi.org/10.1038/s41598-022-12081-z.
[12] A. C. Mohan et al., "Multifaceted properties of Ni and Zn codoped MgO," Sci. Rep. 14 (2024) 13034. doi: https://doi.org/10.1038/s41598-024-83779-5.
[13] P. Desai et al., "Synthesis and dielectric studies of Ni-doped MgO," Adv. Mater. Process. Appl. (2025).
[14] V. Bhoomika et al., "Dual photocatalytic and electrochemical behavior of NiO-doped MgO NPs," Mater. Today: Proc. (2025). doi: https://doi.org/10.1016/j.rechem.2024.101924.
[15] A. Al-Sharabi et al., "Structure, optical properties and antimicrobial activities of MgO," Sci. Rep. 12 (2022) 11134. doi: https://doi.org/10.1038/s41598-022-14811-9.
[16] S. A. Kumar et al., "Facile and Green Synthesis of MgO Nanoparticles," ES Energy & Environment 13 (2021) 13–26.
[17] X. Li et al., "Enhanced antibacterial activity of acid-treated MgO," Front. Microbiol. 12 (2021) 868832. doi: https://doi.org/10.1039/D1RA06221B.
[18] Y. H. Leung et al., "Non-ROS Mediated Toxicity of MgO Nanoparticles," Small 10 (2014) 1171–1183. doi: https://doi.org/10.1002/smll.201302434.
[19] M. A. Zwijnenburg et al., "Effect of particle size on optical/electronic properties of MgO NPs," Phys. Chem. Chem. Phys. 23 (2021) 20685–20696.
[20] CLSI, M02: Performance Standards for Antimicrobial Disk Diffusion, latest accessed 2025; and M100 (2024) tables. doi: https://doi.org/10.1039/D1CP02683F.

*Corresponding author
Mohammed RASHEED,
Applied Sciences Department, University of Technology, Baghdad, Iraq
e-mail: rasheed.mohammed40@yshoo.com

[21] P. R. Jubu et al., “Tauc-plot scale and extrapolation effect on bandgap,” J. Solid State Chem. 292 (2020) 121693. doi: https://doi.org/10.1016/j.jssc.2020.121576.
[22] P. Makuła et al., op. cit. doi: https://doi.org/10.1103/PhysRev.56.978.
[23] S. Landi Jr et al., “Use and misuse of Kubelka–Munk to obtain E_g,” Solid State Commun. 341 (2022) 114574. doi: https://doi.org/10.1016/j.ssc.2021.114573.
[24] M. L. Myrick et al., “The Kubelka–Munk Diffuse Reflectance Formula Revisited,” Applied Spectroscopy 65 (2011) 134–152. doi: https://doi.org/10.1366/10-06161.
[25] CLSI, M100 (Ed.34, 2024) updates. [26] M. Hombach et al., “Standardisation of disk diffusion results,” Clin. Microbiol. Infect. 19 (2013) E255–E263.
[26] S. L. More et al., “Health Effects of Oxidic Nickel Nanoparticles,” Toxicol. Sci. 183 (2021) 1–23. doi: https://doi.org/10.1111/1469-0691.12185.
[27] Y. Mo et al., “Pulmonary effects of nickel-containing nanoparticles,” Front. Toxicol. 6 (2024) 1348896. doi: https://doi.org/10.3389/ftox.2024.1348896.
[28] M. H. Cambre et al., “Cytotoxicity of NiO and $Ni(OH)_2$ NPs,” Int. J. Mol. Sci. 21 (2020) 9436. doi: https://doi.org/10.3390/ijms21249436.
[29] F. Kunc et al., “Physical characterization and cellular toxicity of NiO NPs,” Nanomaterials 12 (2022) 1822. doi: https://doi.org/10.3390/nano12111822.
[30] A. Taşer et al., op. cit. doi: https://doi.org/10.1103/PhysRev.56.978.
[31] A. Almontasser et al., op. cit. doi: https://doi.org/10.1021/acs.jpclett.8b02892.
[32] A. C. Mohan et al., op. cit. doi: https://doi.org/10.1002/smll.201302434.
[33] P. Gaur et al., “Interpretation of Antimicrobial Susceptibility Testing Using Disk Diffusion,” J. Lab. Physicians 15 (2023) 1–10. doi: https://doi.org/10.1039/D1CP02683F.
[34] M. A. Zwijnenburg et al., op. cit. doi: https://doi.org/10.1038/s41598-024-83779-5.
[35] Ruqaya Shaker Mahmood, Rana Jamal Mizban, Mohammed Abdulhadi Sarhan, Ahmed Rashid, Mohammed RASHEED, Tarek Saidani, "Analysis And Applications Of The Beta Prime Distribution In Statistical Modeling", Journal of Positive Sciences, Vol. 3, Issue: 6, pp: 34-41, (2023). doi: https://doi.org/10.52688/ASP61622.
[36] Ruqaya Shaker Mahmood, Rana Jamal Mizban, Mohammed Abdulhadi Sarhan, Ahmed Rashid, Mohammed RASHEED, Tarek Saidani, "Utilizing Beta Distribution For Probabilistic Modeling: Five Numerical Examples", Journal of Positive Sciences, Vol: 3, Issue: 5, pp: 40-48, (2023). doi: https://doi.org/10.52688/ASP42440.
[37] Ahmed Shawki Jaber, Mohammed Abdulhadi Sarhan, Rana Jamal Mizban, Ahmed Rashid, Mohammed RASHEED, Ruqaya Shaker Mahmood, Tarek Diab Ounis, "Modeling Event Occurrences Using the Borel-Tanner Distribution: Applications and Numerical Analysis", Journal of Positive Sciences, Vol.: 3, Issue: 5, pp: 49-55, (2024). doi: https://doi.org/10.52688/ASP31971.
[38] Ruqaya Shaker Mahmood, Rana Jamal Mizban, Mohammed Abdulhadi Sarhan, Ahmed Rashid, Mohammed RASHEED, Tarek Saidani, "Analysis Of Correlated Random Variables Using Bivariate Normal Distribution: Numerical Examples And Applications", Journal of Positive Sciences, Vol. 4, Issue: 1, pp: 28-37, (2024). doi: https://doi.org/10.52688/ASP39921.
[39] Ahmed Shukur, Ahmed Shawki Jaber, Ahmed Rashid, Mohammed RASHEED, Ruqaya Shaker Mahmood, Tarek Diab Ounis, "Application of Bose-Einstein Distribution in Quantum Systems and Statistical Mechanics", Journal of Positive Sciences, Vol. 4, Issue: 2, pp: 27-36, (2024). doi: https://doi.org/10.52688/ASP27315.
[40] Ahmed Shukur, Ahmed Shawki Jaber, Ahmed Rashid, Mohammed RASHEED, Ruqaya Shaker Mahmood, Tarek Diab Ounis, "Application of the Box-Muller Transformation in Generating Normally Distributed Random Variables: A Numerical Approach", Journal of Positive Sciences, Vol. 4, Issue: 3, pp: 32-43, (2024). doi: https://doi.org/10.52688/ASP82349.
[41] Ahmed Shawki Jaber, Taha Rashid, Mohammed RASHEED, Ruqaya Shaker Mahmood, Olfa Maalej, "Analysis of Cauchy Distribution and Its Applications", Journal of Positive Sciences, Vol. 4, Issue: 4, pp: 21-27, (2024). doi: https://doi.org/10.52688/ASP54542.
[42] Taha Rashid, Ahmed Shukur, Mohammed RASHEED, Ruqaya Shaker Mahmood, Olfa Maalej, "Application of the Chi Distribution in Statistical Modeling and Simulation: Numerical Examples and Analysis", Journal of Positive Sciences, Vol. 4, Issue: 4, pp: 28-35, (2024). doi: https://doi.org/10.52688/ASP24189.
[43] Taha Rashid, Mohammed Abdulhadi Sarhan, Ahmed Shukur, Mohammed RASHEED, Ruqaya Shaker Mahmood, Olfa Maalej, "Applications of Chi-Squared Distribution in Hypothesis Testing and Random Variable Analysis", Journal of Positive Sciences, Vol. 4, Issue: 4, pp: 36-45, (2024). doi: https://doi.org/10.52688/ASP 11655.
[44] Mohammed Abdulhadi Sarhan, Mohammed RASHEED, Ruqaya Shaker Mahmood, Taha Rashid, Olfa Maalej, "Evaluating the Effectiveness of Continuity Correction in Discrete Probability Distributions", Journal of Positive Sciences, Vol. 4, Issue: 4, pp: 46-54, (2024). doi: https://doi.org/10.52688/ASP66811.
[45] Ruqaya Shaker Mahmood, "Multivariate Statistical Modeling and Dependence Structures using Copula Distributions", Journal of Positive Sciences, Vol. 3, Issue: 5, pp: 56-63, (2023). doi: https://doi.org/10.52688/ASP80026.
[46] Ruqaya Shaker Mahmood, "Applications of the Difference of Successes Continuous Distribution in Modeling Variability Between Dependent Success Rates", Journal of Positive Sciences, Vol. 4, Issue: 1, pp: 38-46, (2024). doi: https://doi.org/10.52688/ASP80026.
[47] Habiba K. Aity, Muwafaq A. Hasan, Mohammed RASHEED, Ruqaya Shaker Mahmood, Farqad A. Rashid, Zahraa Abbas, Areej A. Hateef, Haider s. Mohammed, Mohammed H. Ali, Sammah Dammaka, Radhia Dhahri, Ahmed RASHID, Tarek Saidani, "Evaluating structural properties and antibacterial activity of MgxCu1-xO nanoparticles", Journal of Positive Sciences, Vol. 4, Issue: 5, pp: 9-19, (2024). doi: https://doi.org/10.52688/ASP72524.

*Corresponding author
Mohammed RASHEED,
Applied Sciences Department, University of Technology, Baghdad, Iraq
e-mail: rasheed.mohammed40@yshoo.com

[48] Habiba K. Aity, Rana A. Hadi, Mohammed RASHEED, Ruqaya Shaker Mahmood, Farqad A. Rashid, Zahraa Abbas, Areej A. Hateef, Haider s. Mohammed, Mohammed H. Ali, Sammah Dammaka, Radhia Dhahri, Ahmed RASHID, Tarek Saidani, "Optical behavior and its role in the antimicrobial properties of MgxCu1-xO nanoparticles", Journal of Positive Sciences, Vol. 4, Issue: 5, pp: 20-29, (2024). doi: https://doi.org/10.52688/ASP66329.

[49] Habiba K. Aity, Ruqaya Shaker Mahmood, Muwafaq A. Hasan, Mohammed RASHEED, Farqad A. Rashid, Zahraa Abbas, Areej A. Hateef, Haider s. Mohammed, Mohammed H. Ali, Sammah Dammaka, Radhia Dhahri, Ahmed RASHID, Nareman Chakchouk, "Exploring the structural features and antimicrobial functionality of Mg0.95Cu0.05O nanoparticles", Journal of Positive Sciences, Vol. 4, Issue: 5, pp: 30-40, (2024). doi: https://doi.org/10.52688/ASP57261.

[50] Habiba K. Aity, Rana A. Hadi, Ruqaya Shaker Mahmood, Mohammed RASHEED, Farqad A. Rashid, Zahraa Abbas, Areej A. Hateef, Ahmed RASHID, Nareman Chakchouk, "The relationship between optical characteristics and antibacterial performance of Mg0.97Cu0.03O nanoparticles", Journal of Positive Sciences, Vol. 4, Issue: 5, pp: 30-40, (2024). doi: https://doi.org/10.52688/ASP33167.

[51] Habiba K. Aity, Kawther A. Alameri, Mohammed RASHEED, Ruqaya Shaker Mahmood, Farqad A. Rashid, Zahraa Abbas, Areej A. Hateef, Ahmed RASHID, Olfa Maalej, "The effect of structure on antibacterial performance of Mg0.94Cu0.06O nanoparticles", Journal of Positive Sciences, Vol. 4, Issue: 6, pp: 1-11, (2024). doi: https://doi.org/10.52688/ASP441661.

[52] Habiba K. Aity, Esra A. Hashem, Mohammed RASHEED, Ruqaya Shaker Mahmood, Farqad A. Rashid, Zahraa Abbas, Areej A. Hateef, Ahmed RASHID, Olfa Maalej, "The role of optical properties in enhancing antimicrobial activity of Mg0.94Cu0.06O nanoparticles", Journal of Positive Sciences, Vol. 4, Issue: 6, pp: 12-22, (2024). doi: https://doi.org/10.52688/ASP19241.

[53] Habiba K. Aity, Mohammed RASHEED, Kawther A. Alameri, Ruqaya Shaker Mahmood, Farqad A. Rashid, Zahraa Abbas, Areej A. Hateef, Ahmed RASHID, Marwa Enneffati, "Structural properties and bacterial inhibition capabilities of Mg0.91Cu0.09O nanoparticles", Journal of Positive Sciences, Vol. 4, Issue: 6, pp: 23-33, (2024). doi: https://doi.org/10.52688/ASP28610.

[54] Habiba K. Aity, Mohammed RASHEED, Esra A. Hashem, Ruqaya Shaker Mahmood, Farqad A. Rashid, Zahraa Abbas, Areej A. Hateef, Ahmed RASHID, Marwa Enneffati, "Assessing Optical Behavior and Antibacterial Potency of Mg0.91Cu0.09O Nanoparticles", Journal of Positive Sciences, Vol. 4, Issue: 6, pp: 34-43, (2024). doi: https://doi.org/10.52688/ASP80838.

[55] Mohammed RASHEED, Ketam K. Khudair, Habiba K. Aity, Ruqaya Shaker Mahmood, Farqad A. Rashid, Zahraa Abbas, Areej A. Hateef, Ahmed RASHID, Taha Rashid, "The impact of optical characteristics on antibacterial properties of Mg0.99Fe0.01O nanoparticles", Journal of Positive Sciences, Vol. 4, Issue: 6, pp: 54-63, (2024). doi: https://doi.org/10.52688/ASP75371.

[56] Mohammed RASHEED, Habiba K. Aity, Ketam K. Khudair, Ruqaya Shaker Mahmood, Farqad A. Rashid, Zahraa Abbas, Areej A. Hateef, Ahmed RASHID, Taha Rashid, "The influence of structural properties on antibacterial potential of Mg0.95Fe0.03O nanoparticles", Journal of Positive Sciences, Vol. 4, Issue: 6, pp: 64-74, (2024). doi: https://doi.org/10.52688/ASP50513.

[57] Ketam K. Khudair, Habiba K. Aity, Ruqaya Shaker Mahmood, Mohammed RASHEED, Farqad A. Rashid, Zahraa Abbas, Areej A. Hateef, Ahmed RASHID, Taha Rashid, "Optical analysis and its impact on antibacterial performance of Mg0.97Fe0.03O nanoparticles", Journal of Positive Sciences, Vol. 4, Issue: 6, pp: 75-86, (2024). doi: https://doi.org/10.52688/ASP88399.

[58] Rafal A. Obayed, Habiba K. Aity, Ruqaya Shaker Mahmood, Mohammed RASHEED, Farqad A. Rashid, Zahraa Abbas, Areej A. Hateef, Ahmed RASHID, Taha Rashid, "Investigating structural traits and their role in antibacterial properties of Mg0.94Fe0.06O nanoparticles", Journal of Positive Sciences, Vol. 4, Issue: 6, pp: 87-96, (2024). doi: https://doi.org/10.52688/ASP75220.

*Corresponding author
Mohammed RASHEED,
Applied Sciences Department, University of Technology, Baghdad, Iraq
e-mail: rasheed.mohammed40@yshoo.com